



Unraveling the adsorption-limited hydrogen oxidation reaction at palladium surface via in situ electron microscopy

Yukun Liu^{a,b,1} , Kunmo Koo^{a,c,1} , Zegang Mao^a, Xianbiao Fu^d , Xiaobing Hu^{a,c} , and Vinayak P. Dravid^{a,b,c,2}

Affiliations are included on p. 9.

Edited by Anatoly Frenkel, Stony Brook University, Stony Brook, NY; received April 25, 2024; accepted August 16, 2024 by Editorial Board Member Joanna Aizenberg

Palladium (Pd) catalysts have been extensively studied for the direct synthesis of H₂O through the hydrogen oxidation reaction at ambient conditions. This heterogeneous catalytic reaction not only holds considerable practical significance but also serves as a classical model for investigating fundamental mechanisms, including adsorption and reactions between adsorbates. Nonetheless, the governing mechanisms and kinetics of its intermediate reaction stages under varying gas conditions remain elusive. This is attributed to the intricate interplay between adsorption, atomic diffusion, and concurrent phase transformation of catalyst. Herein, the Pd-catalyzed, water-forming hydrogen oxidation is studied in situ, to investigate intermediate reaction stages via gas cell transmission electron microscopy. The dynamic behaviors of water generation, associated with reversible palladium hydride formation, are captured in real time with a nanoscale spatial resolution. Our findings suggest that the hydrogen oxidation rate catalyzed by Pd is significantly affected by the sequence in which gases are introduced. Through direct evidence of electron diffraction and density functional theory calculation, we demonstrate that the hydrogen oxidation rate is limited by precursors' adsorption. These nanoscale insights help identify the optimal reaction conditions for Pd-catalyzed hydrogen oxidation, which has substantial implications for water production technologies. The developed understanding also advocates a broader exploration of analogous mechanisms in other metal-catalyzed reactions.

gas phase catalysis | hydrogen oxidation | in situ transmission electron microscopy

Hydrogen oxidation is one of the earliest-known heterogeneous catalytic reactions (1). In addition to its importance in technological applications (2, 3), it also serves as a classic model for investigating fundamental process of the adsorption and reaction of adsorbates on heterogeneous catalysts. Palladium (Pd) is widely used as a heterogeneous catalyst for hydrogenation (4–6) and oxidation reactions (7, 8). The water-forming hydrogen oxidation over Pd surfaces has been extensively investigated in the past through spectroscopy (9–12), atomic force microscopy (AFM) (9, 10, 13), and scanning tunneling microscopy (STM) (14). However, the intermediate steps of this reaction remain not well understood due to the intricate interplay between adsorption and atomic diffusion, which varies with temperature and gas pressure (10, 11, 15). Moreover, hydrogen is known for its ability to easily enter the lattice of Pd and form PdH_x with fast kinetics. This accompanying phase transformation of catalyst further complicates the reaction mechanism of hydrogen oxidation. General characterization techniques limit their analysis to one specific perspective, which prevents a comprehensive understanding of the reaction mechanisms. X-ray diffraction can determine the crystal structure evolution of the catalyst by providing reciprocal space information; however, it cannot quantify the rate of water generation. Spectroscopy-based methods may enable the characterization of the Pd catalyst surface bonding and identify water formation. Nevertheless, these methods do not allow for the simultaneous characterization of the catalyst's structural evolution and the reaction rates. In the case of AFM and STM, while they provide real-space information on the catalyst surface, they lack the capability to characterize hydrogen diffusion into the Pd lattice.

On the other hand, in situ gas cell transmission electron microscopy (GC-TEM) has multimodal analysis capabilities that enable the direct visualization of water formation at nanoscale, structure analysis via electron diffraction, and chemical bonding analysis using electron energy loss spectroscopy (EELS) (16). This facilitates a dynamic analysis of the physical and chemical transformations occurring within the Pd catalyst as it correlates with real-time water formation, thereby providing a comprehensive view of the underlying catalytic processes. Herein, we use in situ GC-TEM equipped with ultrathin silicon nitride microchips (17) to investigate the reaction mechanism of water-forming hydrogen oxidation over the Pd

Significance

Unraveling the reaction kinetics of Pd-catalyzed, water-forming hydrogen oxidation under various gas conditions has posed a considerable experimental challenge. In this study, we achieve nanoscale direct visualization of water formation from this reaction using gas cell transmission electron microscopy. We disentangle the intricate interplay between adsorption, atomic diffusion, and concurrent phase transformation of catalyst. The observed differences in water generation rates with varying gas supply sequences, corroborated by electron diffraction analysis, indicate that the rate of Pd-catalyzed hydrogen oxidation is limited by precursors adsorption. This understanding enables identifying the optimal catalytic reaction condition, holding substantial implications for applications in water generation. Furthermore, our findings advocate exploration of analogous mechanisms in other metal-catalyzed reactions.

The authors declare no competing interest.

This article is a PNAS Direct Submission. A.I.F. is a Guest Editor invited by the Editorial Board.

Copyright © 2024 the Author(s). Published by PNAS. This article is distributed under [Creative Commons Attribution-NonCommercial-NoDerivatives License 4.0 \(CC BY-NC-ND\)](https://creativecommons.org/licenses/by-nc-nd/4.0/).

¹Y.L. and K.K. contributed equally to this work.

²To whom correspondence may be addressed. Email: v-dravid@northwestern.edu.

This article contains supporting information online at <https://www.pnas.org/lookup/suppl/doi:10.1073/pnas.2408277121/-/DCSupplemental>.

Published September 27, 2024.

nanoparticles under different gas conditions. Compared to open-cell environmental TEM, the GC-TEM offers the advantage of adjustable cell pressure from high vacuum to above atmospheric pressure (16). The wide range of available gas pressure enables the controllable formation of both hydrogen-poor α -phase and hydrogen-rich β -phase of PdH_x at room temperature (18). These experimental conditions are crucial for simulating real-world catalytic reactions. The water formation process, starting with H₂ and O₂ gases, was monitored in real time under a controlled environment over the Pd surface. The observed nanobubbles were confirmed to be water through a combination of EELS analysis and heating experiments.

Furthermore, theoretical calculations and electron diffraction-based structural analysis were employed to understand the evolving kinetics of water formation under different gas conditions. Our findings suggest that the reaction rates of Pd-catalyzed water formation significantly differ between scenarios when H₂ and O₂ are introduced to Pd nanoparticles sequentially versus concurrently. Density functional theory (DFT) calculation reveals that dissociated H atoms can easily enter the Pd matrix and form PdH_x in the absence of O₂, which is evidenced by the expanded lattice parameters identified through electron diffraction. However, exposing Pd to H₂ concurrently with O₂ prevents the formation of PdH_x. This is because O atoms preferentially occupying surface octahedral sites on Pd significantly increase the energy barrier for the adsorption and diffusion of dissociated H atoms into Pd lattice, as supported by the observed invariant lattice parameters. The increased energy barrier restricts the continuous supply of the

hydrogen precursor necessary for the water formation reaction, thereby reducing the reaction rate. These nanoscale insights facilitate the identification of optimal reaction conditions for Pd-catalyzed hydrogen oxidation, which holds significant implications for water production applications at ambient conditions. Furthermore, the developed understanding of the interplay between adsorption and diffusion mechanisms across different atomic species in metal catalysts advocates further exploration of analogous mechanisms in other metal-catalyzed reactions.

Results and Discussion

In Situ Pd-Catalyzed Water-Forming Hydrogen Oxidation. The water-forming hydrogen oxidation catalyzed by Pd consists of two stages: dissociative adsorption and reaction (9–11). In the dissociative adsorption stage, H and O atoms competitively occupy the open surface sites of Pd after dissociation. The adsorbed atoms then diffuse across the Pd surface and react to form H₂O. The Pd used in a typical in situ GC-TEM experiment for catalyzing hydrogen oxidation are nanocubes, approximately 20 nm in size, with (100) surfaces exposed (19). The Pd nanocubes are highly crystalline evidenced by the electron diffraction pattern which is overlapped with simulation in Fig. 1B. To avoid the interference from surface oxides, the surfaces of Pd nanocubes were examined using atomic resolution high-angle annular dark field (HAADF) imaging. A typical Pd nanocube is shown in Fig. 1C, which is highly crystalline and free of surface oxide and ligands.

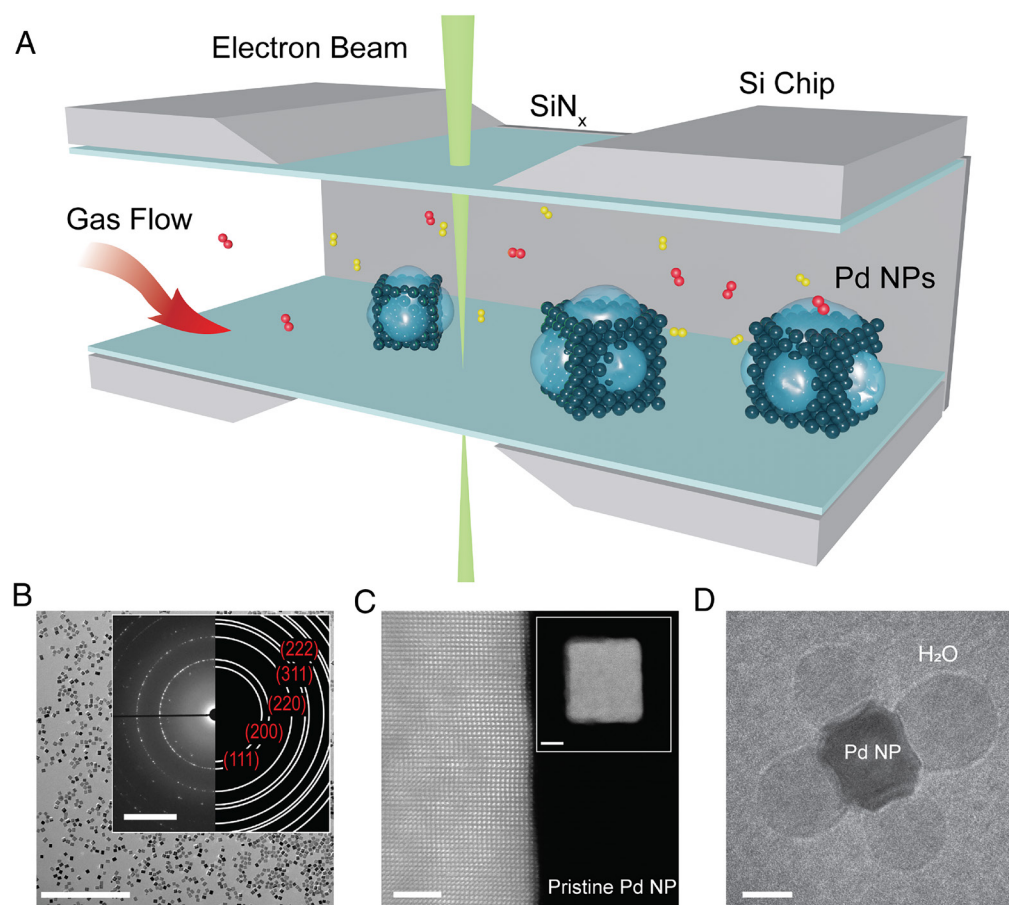


Fig. 1. Pd nanoparticle catalyzed hydrogen oxidation reaction. (A) Schematic illustration of in situ gas cell TEM for H₂O nanobubble generation from Pd-catalyzed hydrogen oxidation reaction. Red molecules refer to O₂ while yellow molecules refer to H₂. (B) Low magnification BF image of pristine cubic Pd nanoparticles with their electron diffraction pattern as an inset. The size of the Pd nanoparticle is around 20 nm. (Scale bar, 500 nm and Scale bar (inset), 5 nm⁻¹.) (C) HRSTEM HAADF image of a representative Pd nanoparticle. No oxide layer was observed on the surface of the nanoparticle. (Scale bar, 2 nm and Scale bar (inset), 5 nm.) (D) BF image of H₂O bubble formation on the surface of Pd nanoparticle after flowing H₂ and O₂ in sequence. (Scale bar, 5 nm.)

In the water-forming hydrogen oxidation process, Pd nanocubes were pre-exposed to 1 atm pressure of H_2 gas for 10 min to allow H atoms to occupy the open surface sites and diffuse into lattice (Fig. 1A). Once saturated with H atoms and transformed into PdH_x , the nanocubes were then subsequently supplied with 1 atm of O_2 to provide an oxygen precursor for the hydrogen oxidation reaction. During the O_2 supply stage, H_2O bubbles continuously formed at the (100) surfaces of Pd nanocubes from the hydrogen oxidation (Fig. 1D). *SI Appendix, Fig. S1* shows a TEM image series of a water-forming process, where nanobubbles of H_2O nucleated at the (100) surfaces of nanocubes. The schematic in *SI Appendix, Fig. S2* illustrates the cross-sectional view of the nanobubble expansion. The nanobubble consists of a liquid-phase water film on its surface and encapsulated gas within. This is supported by the spatially uniform contrast within each nanobubble, which indicates a relatively homogenous thickness of liquid-phase layer. This stands in contrast to water droplets, which would exhibit thickness and contrast gradient. Furthermore, the observation of multiple water film layers within nanobubbles also supports that they are not entirely filled internally, a point that will be elaborated upon later. After nucleation, the nanobubbles steadily grew because of the water generation from the ongoing hydrogen oxidation reaction. In the meantime, the H_2 gases were also progressively released from the PdH_x lattice to fill the nanobubble with produced gas phase H_2O . Upon contact, nanobubbles coalesced (*SI Appendix, Fig. S3*) and transformed from semiellipsoids toward spheres, driven by the surface tension. The growth of nanobubbles continued until they collapsed upon reaching a critical size, where the surface tension can no longer balance the internal pressure difference of nanobubbles (*SI Appendix, Fig. S1*) (20).

Identification of Water Generation. Pd-catalyzed hydrogen oxidation typically involves numerous parallel and consecutive reactions, resulting in the production of either H_2O or H_2O_2 (21, 22). While the formation of H_2O is thermodynamically more favorable (23), it is crucial to determine the chemical identity of the generated nanobubbles to eliminate other possibilities. Here, we utilized EELS and conducted in situ heating experiments to identify the composition of generated nanobubbles, based on their chemical bonding and boiling point. It is worth noting that a residual gas analyzer (RGA) is less applicable in this case since the generated water is mostly entrapped in the liquid film on bubble surfaces rather than flowing to the gas outlet. Moreover, water vapor is one of the main residual gases in the apparatus even after evacuation, as it can strongly bind to surfaces. Therefore, peaks corresponding to water vapor are always present in the RGA spectrum, making it difficult to distinguish them from the catalytic product. The peak intensity contributed by parasitic water is generally much larger than that of the evaporated water vapor from the nanobubbles, which limits the application of RGA in identifying water generation (24).

We conducted EELS analysis on the generated nanobubbles, enabled by the equipped ultrathin SiN_x membrane. The typical nanobubbles after coalescence are demonstrated in *SI Appendix, Fig. S4A*, where they can reach sizes of approximately 50 nm and attach to one (100) surface of a Pd nanocube, as shown in *SI Appendix, Fig. S4B*. In the HAADF image (Fig. 2A), these nanobubbles exhibit a darker contrast due to the relatively lower atomic number compared with Pd. The supply of H_2 and O_2 gases was discontinued before the EELS analysis to halt the reaction, and the gas cell was evacuated to maintain a gas pressure of less than 0.1 torr to eliminate the interference from residual gases with the EELS signal. Fig. 2B presents a representative EELS analysis

on the nanobubbles and SiN_x membrane, with the EELS representing area-averaged results from the highlighted regions in the HAADF image. To detect the presence of H_2O formation, our analysis focused on the energy loss range of 500 to 580 eV for the O K -edge. Region I serves as a background reference, representing SiN_x membrane area, which is devoid of nanobubbles and Pd nanoparticles. In this region, the acquired spectrum revealed an extended-fine-structure peak with a sharp onset at 532 eV. This edge feature arises from the O K -edge of SiO_2 , which has been identified as a result of O–O scattering (25, 26). The formation of SiO_2 was induced by the plasma treatment on the SiN_x membrane during the fabrication process, where oxygen from the plasma can substitute the nitrogen in the SiN_x , and the depth of resultant SiO_2 can reach to the order of ten nanometers (27). The EELS of the O K -edge acquired ex situ on the SiN_x membrane under vacuum is also shown in *SI Appendix, Fig. S5* as a reference. In comparison, the EELS acquired at regions II–V are representative of nanobubbles. Notably, an additional peak feature emerges at 537 eV in the EELS of nanobubble (II–V) when compared to the reference spectrum (I). This particular feature is a characteristic of the EELS of H_2O . The observed energy loss corresponds to electronic transitions in H_2O from O $1a_1$ state into the Rydberg orbitals at high energies, typically manifested as a pronounced pre-edge peak at 535 eV, an enhancement at the bottom of conduction band (537 eV), and a less distinct structure in the continuum (542 eV) (28–30). However, the peak features at 535 eV and 542 eV are less evident due to relatively large sample and membrane thickness (31) and their overlap with the core loss O K -edge of the SiO_2 , which is located at the top and bottom membranes of the gas cell. The EELS acquired from another nanobubble are shown in *SI Appendix, Fig. S6*, where they demonstrate similar features in the O K -edge. The identified electronic structure features provide direct evidence that the generated nanobubbles are H_2O (32).

In addition to chemical analysis through spectroscopy, we also implemented in situ heating experiment to identify the boiling point of nanobubbles for physical characterization. H_2O and H_2O_2 have distinct boiling points; H_2O evaporates at approximately 100 °C, while H_2O_2 evaporates at 150 °C under standard atmospheric pressure (33). This distinction allowed us to differentiate between them and to confirm the product of the reaction in the heating experiment. The gas supply of 1 atm O_2 remained constant during the heating experiment to maintain the target nanobubble and provide a gas pressure resembling ambient environment. Fig. 2C displays a series of TEM images showing the evolution of the nanobubble during the heating experiment, with a heating rate of approximately 0.5 °C/s. The corresponding heating profile is presented in Fig. 2D. The initial size of the nanobubble was approximately 36 nm in diameter, and it experienced progressive growth to reach approximately 74 nm at $t = 180$ s. The contour evolution, describing this growth, is demonstrated in Fig. 2E, illustrating a continuous expansion. This volume expansion is induced by both the continued hydrogen oxidation reaction and the continuous release of residual H_2 from the PdH_x due to the decreased H atom solubility at elevated temperature (34). The continuous hydrogen oxidation reaction generated an increased amount of water, partially contributing to the further expansion of the water film. In the heating process, a second circular outline emerged within the nanobubble (*SI Appendix, Fig. S7*), which is another layer of liquid water film formed and expanded to merge with the existing layer. This phenomenon directly supports that the generated water is in the form of nanobubble, as depicted in *SI Appendix, Fig. S2*. Once the environmental temperature reached approximately 100 °C

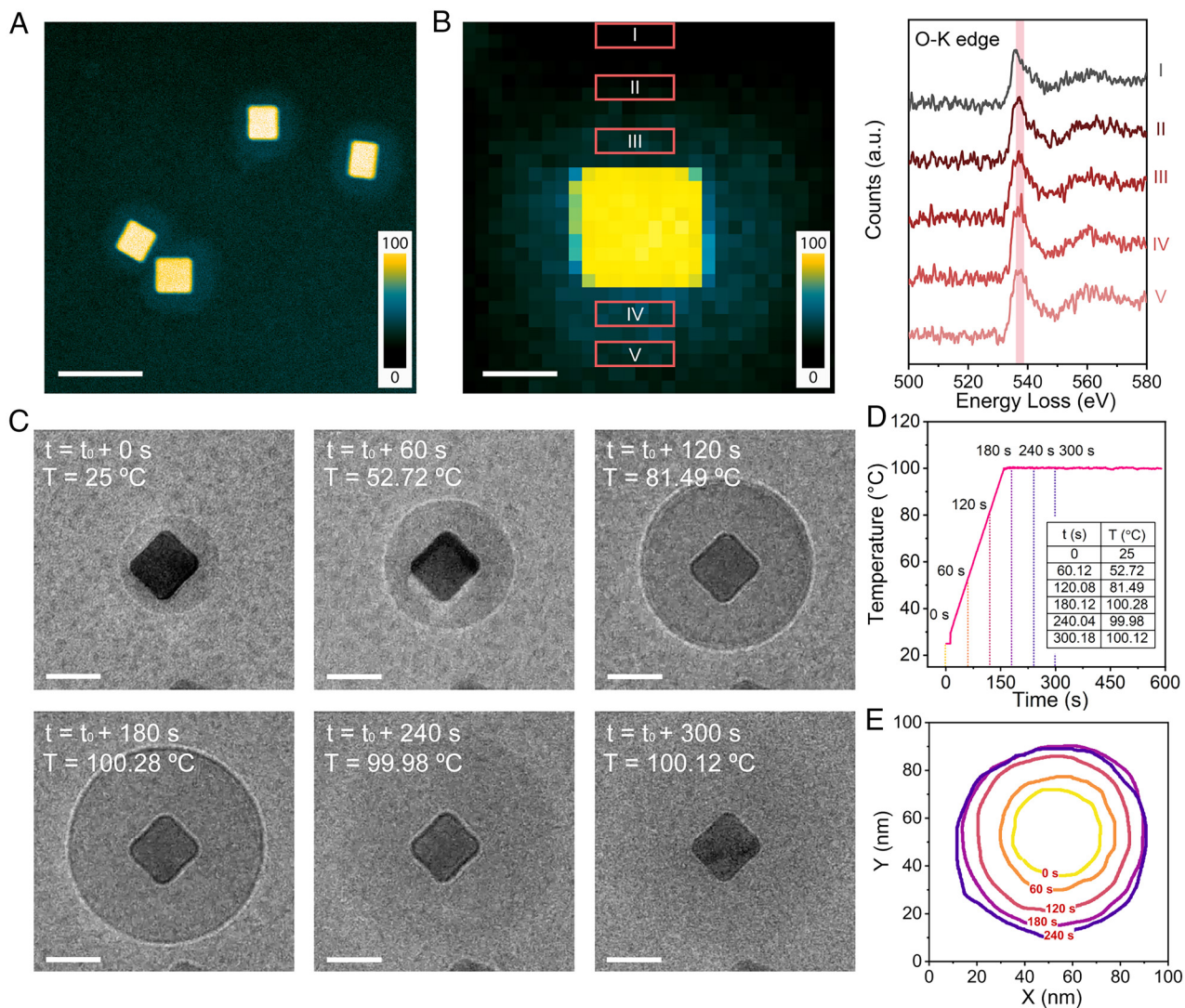


Fig. 2. Chemical and thermal analysis of nanobubble post hydrogen oxidation reaction (A) HAADF image of Pd nanocubes encapsulated by generated H₂O nanobubbles. (Scale bar, 50 nm.) (B) EELS analysis of the Oxygen K-edge of formed H₂O nanobubbles and SiN_x membrane. (Scale bar, 10 nm.) (C) TEM images series of H₂O nanobubble evaporation during in situ heating, with the temperature profile shown in (D) and the contour evolution of nanobubbles demonstrated in (E). (Scale bar, 20 nm.)

($t = 180$ s), the vapor pressure of the liquid-phase water film became equivalent to the environmental pressure, leading to evaporation ($t = 240$ s). As revealed by Fig. 2C (Movie S1), the nanobubble evaporated at 240 s, reflecting the disappearance of the bubble outline. The remaining H₂O diffused into the environment, and the contrast progressively decreased. The evaporation of H₂O did not lead to any observable solid residues, which implies none of salt or carbonaceous species was contained by the bubble. This observed boiling point near 100 °C in combination with EELS analysis confirms the generated nanobubbles are H₂O.

Kinetics of Pd-Catalyzed Hydrogen Oxidation. The Pd-catalyzed hydrogen oxidation involves multiple intermediate steps in which adsorption and diffusion of H and O atoms occur concurrently. This concurrent process poses challenges in understanding the reaction kinetics. Leveraging the capabilities of direct visualization and simultaneous structural and chemical analysis provided by GC-TEM, we further investigate the kinetics of Pd-catalyzed hydrogen oxidation by examining the role of adsorption and diffusion under three different gas conditions: A) pre-exposure to 1 atm H₂ followed by 1 atm O₂ supply, B) exposure to 1 atm

mixed H₂ and O₂, and C) pre-exposure to 1 atm O₂ followed by 1 atm H₂ supply.

Fig. 3 illustrates the generation of nanobubbles from hydrogen oxidation under these three gas conditions, and a significant difference in reaction kinetics was observed. In condition A, Pd nanocubes were pre-exposed to 1 atm of H₂ for 10 min before being supplied with 1 atm of O₂ to initiate the hydrogen oxidation reaction. This pre-exposure allowed dissociated H atoms to adsorb onto and diffuse into Pd nanocubes without interference from the O atoms. Consequently, the adsorption and diffusion processes of H and O atoms were isolated, and the reaction kinetics were constrained by the adsorption of O atoms onto the Pd surface already covered by H atoms and their subsequent diffusion. After the Pd was saturated with H atoms and formed PdH_x, O₂ gas was supplied to provide oxygen precursor. As depicted by Fig. 3A (Movie S2), hydrogen oxidation occurred at a rapid rate, with nanobubbles beginning to nucleate at the facets of multiple Pd nanocubes ($t = 43$ s) and undergoing continuous growth until collapse. The TEM image was acquired from a region that was not exposed to the electron beam after the reaction, to evaluate the electron beam effect. As shown in SI Appendix, Fig. S8, the highlighted field-of-view (FOV) area corresponds to the same region

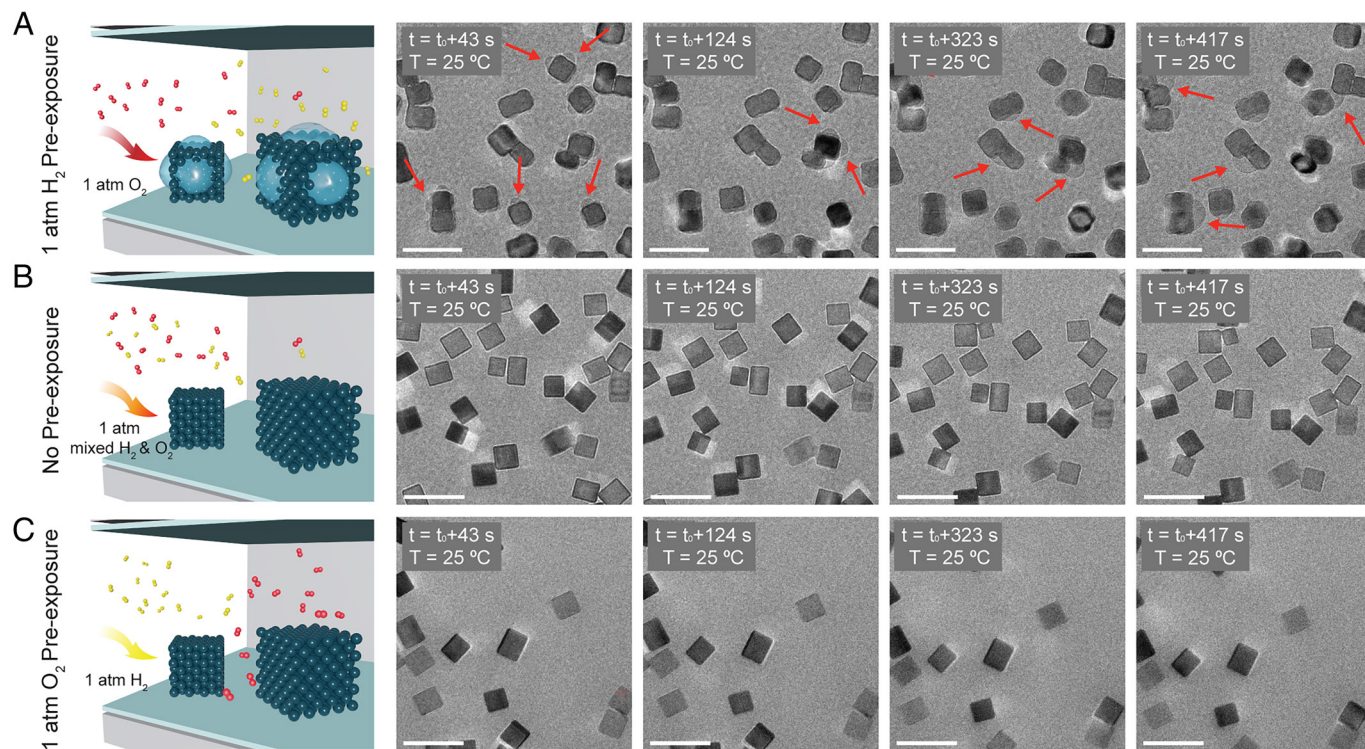
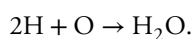


Fig. 3. Influence of gas precursor supply sequence on the kinetics of Pd-catalyzed hydrogen oxidation. TEM image series of (A) Pd nanocubes supplied with 1 atm of O_2 gas after being pre-exposed to 1 atm of H_2 gas. H_2O nanobubble rapidly nucleated at the (100) surface of Pd nanocubes and continuously grew until they collapsed due to radiolysis. (B) Pd nanocubes supplied with 1 atm of mixed H_2 and O_2 gas with equal volume ratio. No H_2O nanobubble formation was observed. (Scale bar, 50 nm in all images.) (C) Pd nanocubes supplied with 1 atm of H_2 gas after being pre-exposed to 1 atm of O_2 gas. No H_2O nanobubble formation was observed. In the schematic, red molecules refer to O_2 while yellow molecules refer to H_2 .

as in Fig. 3A, where data acquisition was performed under gas condition A. Outside the FOV, where Pd nanoparticles were not exposed to the electron beam, water bubbles still formed on the Pd surface. This indicates that the observed Pd-catalyzed hydrogen oxidation reaction is not induced by the electron beam; rather, the electron beam effect on the reaction is negligible.

The reaction rate can be evaluated by the size expansion of generated nanobubbles. To obtain a more accurate evaluation, we identified a nanobubble growth process where coalescence occurred. In this growth process, all continuously generated nanobubbles merged into a larger bubble, which can be approximated as a sphere (SI Appendix, Fig. S9 and Movie S2). Thus, the volume of the generated water can be approximated by $dV = Adr$, as the liquid-phase water is concentrated on the thin film located at the bubble surface. Here, V represents the volume of the generated water, A denotes the surface area of the bubble, and r stands for the thickness of the liquidous water shell. The thickness of the water film can be considered constant, as the contrast of the nanobubble remains unchanged during growth. Consequently, the generated water concentration, $[H_2O]$, is proportional to the surface area A of nanobubble. SI Appendix, Fig. S9B shows the surface area, A , plotted against time. The trend reveals a first-order reaction with respect to $[H]$, where the experimental data can be fitted based on the integrated rate law. The details of the derivation are shown in SI. The water generation reaction can be described as



The reaction rate of this first-order reaction (10) is then given as

$$\frac{d[H_2O]}{dt} = a[H].$$

Here, a is a rate constant. Given that oxygen was continuously supplied under reaction condition A, the reaction rate can be approximated as being independent of the oxygen concentration, $[O]$, making the reaction order with respect to $[O]$ effectively pseudozeroth. This aligns with our observation that the reaction rate depends on the supply of H precursor that is stored in PdH_x lattice, which will be discussed later.

In comparison, reaction condition B introduced a 1 atm mixture of H_2 and O_2 gases, each with equal partial pressures, to Pd nanocubes. However, despite the abundance of both hydrogen and oxygen precursors compared to condition A, only trace amounts of nanobubble generation were observed (Fig. 3B). This suggests that the hydrogen oxidation reaction rate under condition B was significantly slower than that under condition A. This discrepancy raises the question of why the reaction rate was substantially slower under the mixed precursor condition despite their abundance. In addition to the difference in precursor abundance, another major difference between conditions A and B is the adsorption of H and O atoms to Pd surface, influenced by gas supply sequence. By pre-exposing Pd nanocubes to H_2 gas under condition A, dissociated H atoms were able to adsorb to Pd surfaces without interference from O atoms. Consequently, Pd nanocubes were saturated with H atoms before further introducing O_2 gas. In contrast, introducing a mixture of H_2 and O_2 gases under condition B led to dissociated H and O atoms freely competing for surface site occupancy. The resulting surface occupancy was determined by the relative adsorption energies of the different atomic species. Therefore, these differences suggest that the adsorption of O atoms to Pd surface was likely responsible for the observed reaction rate difference between conditions A and B.

To further verify the role of oxygen surface occupancy in reaction rates, condition C reserved the gas sequence by pre-exposing Pd nanocubes to 1 atm of O_2 . As a result, the Pd surface became

saturated with O atoms, and the reaction kinetics were primarily governed by the rate of H atom adsorption and diffusion. Similar to condition B, when 1 atm of H₂ was introduced to these pre-exposed Pd nanocubes, no obvious nanobubble generation was observed within the observation period (Fig. 3C). Subsequent electron diffraction analysis demonstrated that H atoms were blocked from the Pd surface due to the presence of occupied O atoms, which will be discussed later. The pronounced difference in nanobubble generation rates among the three gas conditions highlights that the reaction kinetics are influenced by the changes in adsorption and diffusion behavior of H and O atoms on Pd surface under varying gas conditions. Specifically, the consistently low reaction rate observed in conditions B and C suggests that the occupation of O atoms at the Pd surface impedes H atom adsorption and interlattice diffusion, thereby reducing the overall reaction rate.

To gain a fundamental understanding of the observed reaction kinematics of Pd-catalyzed hydrogen oxidation, we investigated the diffusion and adsorption energy barrier for H atoms by using DFT to simulate these processes during the reaction. Pd crystallizes in a cubic structure with a $Fm\bar{3}m$ space group, containing four atoms in each unit cell accompanied by 4 octahedral and 8 tetrahedral interstitial sites (Fig. 4A). We first examined the diffusion mechanism of H atoms inside a pristine Pd nanoparticle. From an energetic perspective, H atoms prefer occupying octahedral interstitial sites over tetrahedral interstitial sites, evidenced by a lower energy state with 0.04 eV energy offset. This preference is attributed to the larger radius of the octahedral sites, $R_{\text{Octahedral}} = (\sqrt{2}-1)r$, compared to the tetrahedral sites, $R_{\text{Tetrahedral}} = \left(\frac{\sqrt{6}}{2}-1\right)r$, where r represents the radius of the host

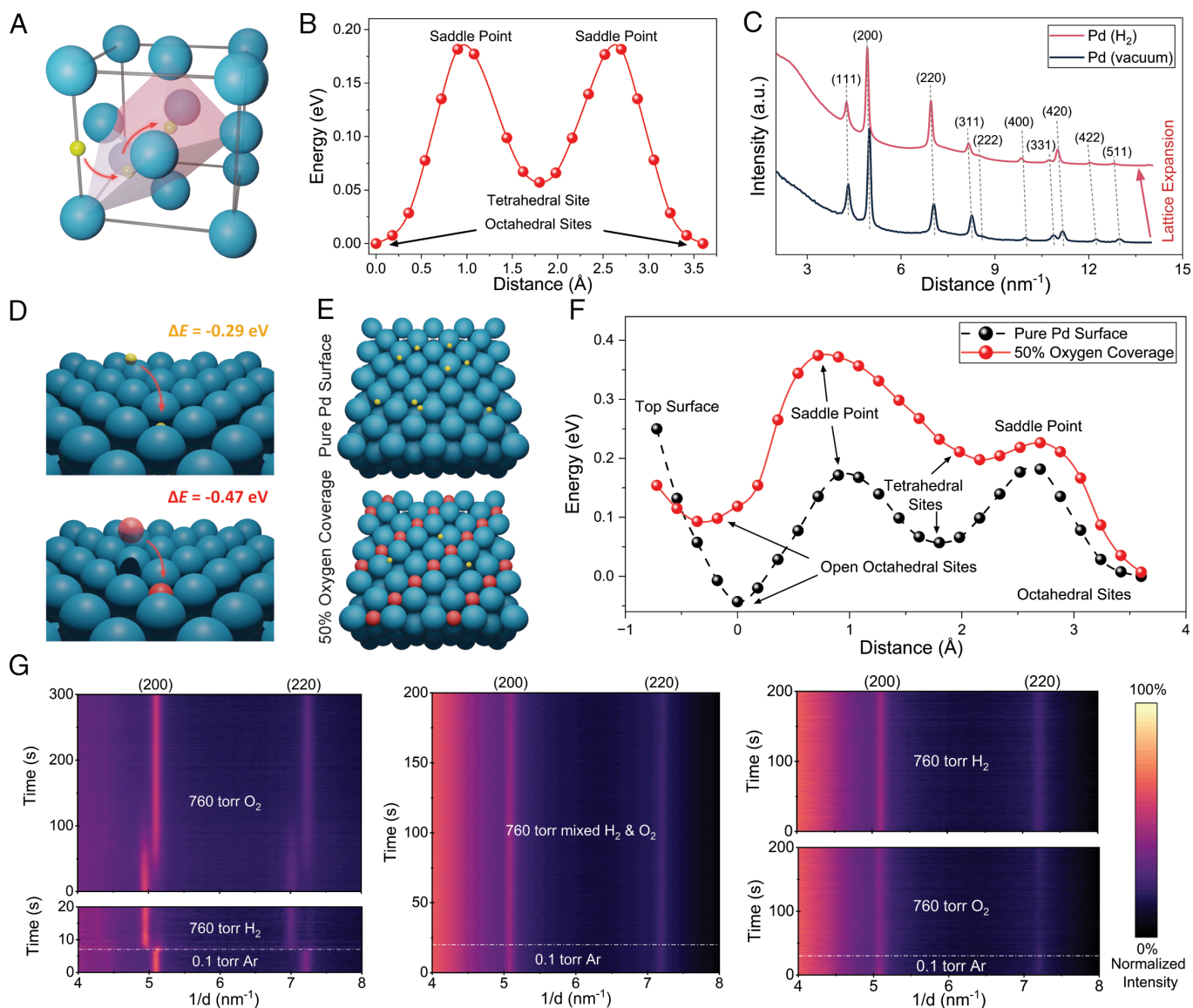


Fig. 4. Adsorption and diffusion mechanism of dissociated H atoms under different gas conditions. In the schematic illustration, blue spheres represent Pd atoms, yellow spheres represent H atoms, while red spheres represent O atoms. (A) Schematic illustration of H atom diffusion within the pristine Pd lattice. H atoms migrate through moving between octahedral and tetrahedral interstitial sites. (B) The calculated energy path of H atom diffusion within the pristine Pd lattice. (C) The radial profile of electron diffraction pattern acquired on Pd nanocubes in vacuum and under 1 atm of H₂, respectively. The infusion of H atoms into Pd lattice led to lattice expansion. (D) The adsorption energy of H and O atoms on the open octahedral sites of Pd surface. (E) Schematic illustration of H atom adsorption on open octahedral sites of Pd surface with and without O atom preoccupation. (F) The calculated energy paths of H atom adsorption and diffusion from surface of Pd under the conditions described in (E). (G) The radial profiles of in situ electron diffraction patterns acquired on Pd nanocubes under different gas supply conditions.

atom Pd (Fig. 4A). H atoms occupying the smaller tetrahedral sites experience strain due to lattice distortion, whereas those in octahedral sites are less affected and exhibit lower energy. The minimum local energy pathway for hydrogen diffusion was calculated using the nudged elastic band (NEB) method. The diffusion path of H atoms starts from the energetically favored octahedral sites, proceeds to the smaller tetrahedral sites, and then migrates to the next octahedral site (Fig. 4B). The energy barrier for this migration path, also referred to as the saddle point energy, is calculated to be 0.18 eV. Such a low migration barrier enables rapid diffusion of H atoms within the Pd lattice and quick saturation of the interstitial sites. This diffusion of H atoms into the Pd lattice leads to the formation of PdH_x, which is a reversible reaction driven by the H₂ pressure in the environment (16). The formation of palladium hydride can be readily identified by electron diffraction, as the incorporation of H atoms into interstitial sites results in lattice expansion (35). When Pd nanocubes were exposed to 1 atm H₂ gas, the lattice parameters of the Pd crystal expanded by approximately 2.6%, as revealed by a peak shift in the radial profile of the electron diffraction pattern (Fig. 4C and *SI Appendix*, Fig. S10). Therefore, this lattice expansion can be utilized to confirm the occurrence of the adsorption and diffusion of H atoms into Pd lattice. This adsorption and diffusion process is not affected by the electron beam. *SI Appendix*, Fig. S11 shows a beam-off experiment where the diffraction patterns were acquired on Pd nanocubes before (*Left*) and after exposure to 760 Torr H₂ (*Right*) without being exposed to electron beam during gas flow. The lattice expansion behavior is consistent with the beam-on condition (Fig. 4C and *SI Appendix*, Fig. S9). Therefore, the electron beam-induced effect on gas adsorption and diffusion is negligible.

The adsorption mechanism of dissociated H atoms onto Pd nanoparticles highly depends on the surface occupation states. To explore how various gas conditions affect the surface site occupation of Pd nanocubes, and consequently impact H atom adsorption and diffusion, a model of the (100) Pd surface with exposed octahedral sites was constructed (*SI Appendix*, Fig. S12). On a pure (100) Pd surface, the energy of dissociated H atoms situated on open Pd octahedral sites is 0.29 eV lower than when positioned in the vacuum above the Pd surface (Fig. 4D). Therefore, dissociated H atoms are able to adsorb onto octahedral sites on the Pd surface and subsequently diffuse into the Pd lattice (Fig. 4E). The diffusion of H atoms from the Pd surface follows the same path as the internal diffusion (i.e., from octahedral to tetrahedral sites and back to octahedral sites, etc.), however, the energetic landscape differs slightly. The energy level of H atoms at open octahedral sites on the surface (Fig. 4F) is 0.04 eV lower than that of those at internal octahedral sites. Meanwhile, the energy of the first saddle point is 0.1 eV lower than the saddle point for internal diffusion (Fig. 4B). Thus, it can be concluded that the diffusion of H atoms from the Pd surface into internal interstitial sites occurs much faster than diffusion within the Pd lattice, and this process happens spontaneously when H₂ gas is supplied to the Pd nanocubes.

However, the energy pathway for H atoms' diffusion will be significantly altered if the open octahedral sites on the Pd surface are preoccupied by oxygen atoms. In the scenario where 50% of the open octahedral sites are occupied by O atoms (Fig. 4E), the energy level of H atoms positioned atop the Pd surface is reduced, becoming 0.01 eV lower than that of a pure Pd surface. More importantly, the local energy minimum for H atoms is not located at the open octahedral site but rather 0.35 Å above it. This suggests that the adsorption of H atoms onto a Pd surface with 50% of its octahedral sites covered by O atoms is energetically less favorable

and not spontaneous. Moreover, as H atoms move from the open octahedral sites to the first saddle point, their energy level increases to 0.37 eV, which is 0.20 eV higher than the saddle point energy on a pure Pd surface. When H atoms move to the nearest tetrahedral sites, the energy level reaches 0.23 eV, which does not represent a local energy minimum state, unlike what is observed on the pure Pd surface. The energy of the second saddle point remains slightly higher until the H atoms reach an internal octahedral site, at which point it aligns with the internal diffusion scenario. The significantly increased energy barrier and the shift in the position of the local energy minimum suggest that the diffusion of H atoms from the surface into the Pd lattice is energetically disfavored when 50% of the octahedral sites on the (100) Pd surface are occupied by O atoms. Furthermore, when 100% of the open octahedral sites are occupied by O atoms, no diffusion pathway remains for H atoms to enter the Pd lattice. Consequently, H atoms remain above the Pd surface and the reaction is halted.

The changes in the energy path of H atoms adsorption and diffusion, caused by Pd surface occupation by O atoms, elucidate the observed differences in reaction kinetics under varying gas conditions. In reaction condition A, when Pd nanocubes were pre-exposed to H₂, the dissociated H atoms readily adsorbed onto the pristine Pd surface and rapidly diffused into the lattice due to the low energy barrier. Electron diffraction analysis (Fig. 4G and *Movie S3*) was conducted to support these findings. Upon exposure of Pd nanocubes to H₂ gas, the rapid infusion of H atoms into the Pd lattice led to an almost instant lattice expansion of 2.6%, with the (200) diffraction peaks in the radial profile shifting from 5.08 nm⁻¹ to 4.95 nm⁻¹. Following the saturation of the Pd lattice with H atoms, the introduction of 1 atm of O₂ initiated hydrogen oxidation. The dissociated O atoms adsorbed onto the Pd surface and reacted with H atoms to form H₂O nanobubbles. This reaction consumed the H atom occupying the Pd surface sites, while internal H atoms diffused toward the surface to continue the reaction with available oxygen precursor. As the concentration of H atoms in the PdH_x decreased due to the reaction, the PdH_x crystals progressively transformed back to Pd, exhibiting reduced lattice parameters. This transformation is evidenced in the radial profile of electron diffraction, where another diffuse peak for the contracted (200) plane appeared at 1/d = 5.10 nm⁻¹ (*t* = 70 s), coexisting with the original (200) peak at 1/d = 4.95 nm⁻¹. The hydrogen oxidation reaction proceeded at varying rates across the field of view; thus, some PdH_x nanocubes depleted their stored H atoms faster and reverted to Pd crystals with smaller lattice parameters, while others remained as PdH_x due to slower reaction rates. By *t* = 170 s, all PdH_x nanocubes had completed the reactions and transformed back into Pd nanocubes. The rapid infusion of dissociated H atoms and their subsequent discernible consumption account for the rapid reaction rates in hydrogen oxidation reactions (Fig. 3A). The same gas conditions (condition A) were implemented on Au nanocubes as a controlled experiment (*SI Appendix*, Fig. S13A and *Movie S4*). Electron diffraction analysis (*SI Appendix*, Fig. S13B and *Movie S5*) indicates the lattice parameters of Au nanocubes remained invariant, moreover, no nanobubble generation was observed, as shown in *SI Appendix*, Fig. S13 C and D. This controlled experiment excludes the possibility that nanobubble was generated from the environment.

In contrast, under reaction condition B, a mixture of H₂ and O₂ gases was simultaneously supplied to Pd nanocubes with equal partial pressure. The energy level of O atoms adapting to the octahedral sites on the Pd surface is calculated to be 0.47 eV lower than that atop the Pd surface (Fig. 4D). In contrast, H atoms exhibited a much weaker affinity ($\Delta E = -0.29$ eV). As a result, the surface octahedral sites on Pd were either immediately fully

occupied by O atoms or still had very few sites occupied by H atoms. In the latter scenario, a localized hydrogen oxidation reaction might occur, consuming H atoms and creating open sites in the process. Consequently, dissociated H and O atoms continue to compete for the open sites at Pd surface. After reaching equilibrium, the Pd surface was ultimately saturated with O atoms due to their larger affinity for adsorption. However, due to their large atomic radius, adsorbed O atoms were unable to further diffuse into the Pd lattice through tetrahedral interstitial sites. As a result, they remained at the Pd surface. Despite the abundance of hydrogen supply in the environment, the presence of O atoms at the surface octahedral sites increased the energy barrier for their subsequent adsorption and diffusion to Pd lattice. As indicated by the electron diffraction radial profile (Fig. 4G), no significant peak shifts were observed, suggesting that H atoms were hindered by O atoms at surface octahedral sites and could not efficiently enter Pd lattice to initiate the hydrogen oxidation reaction. Consequently, no obvious H₂O nanobubble formation was observed under gas condition B.

Similarly, when Pd nanocubes were pre-exposed to 1 atm of O₂ gas under condition C, the strong affinity of O atoms for the octahedral sites on the Pd surface ($\Delta E = -0.47$ eV) resulted in the Pd surface becoming saturated with O atoms. After subsequently introducing 1 atm of H₂, no surface sites remained available for dissociated H atoms to occupy, thereby preventing the initiation of the reaction. This phenomenon is substantiated by the invariant lattice parameters observed in the electron diffraction radial profile (Fig. 4G). As a result, the hydrogen oxidation reaction was similarly suppressed in condition C. These electron diffraction analyses provide direct evidence to corroborate the theoretical calculation results on the adsorption and diffusion behaviors of H and O atoms to Pd nanocubes. Combined with the observed reaction rate difference, the surface adsorption and internal diffusion of H and O atoms have been identified to be the crucial factor in determining the kinetics of Pd-catalyzed hydrogen oxidation reaction.

In summary, we have presented direct visualization of the H₂O generation from Pd-catalyzed hydrogen oxidation using in situ GC-TEM and have investigated its reaction kinetics under various gas conditions. Our results demonstrate that the reaction rate of hydrogen oxidation is highly dependent on the sequence in which gas precursors are supplied. As illustrated in *SI Appendix, Fig. S14*, pre-exposing Pd nanocubes to H₂ gas facilitates the infusion of dissociated H atoms into the lattice and the formation of PdH_x with expanded lattice parameters. This is driven by the low energy barrier for H atom adsorption and diffusion into pristine Pd. These incorporated H atoms in the Pd interstitial sites diffused to the surface, initiating and continuously serving as precursors for the rapid hydrogen oxidation reaction once O₂ is introduced. Conversely, reversing the gas supply sequence or introducing a mixture of H₂ and O₂ results in much slower or even undetectable reactions. This is attributed to the fact that dissociated O atoms exhibit a much lower adsorption energy to the Pd surface octahedral sites compared to H atoms; hence, they preferentially occupy these sites. Their presence significantly increases the energy barrier for H atom adsorption and diffusion, interrupting the supply of the hydrogen precursor for the oxidation reactions and thus leading to diminished reaction rates. These insights into the complex interplay between adsorption, diffusion, and catalytic reaction in Pd-catalyzed hydrogen oxidation have important implications for optimizing reaction conditions for water generation applications. Moreover, this finding also advocates broader exploration of other metal-catalyzed reactions that might share analogous mechanisms, as well as further investigation into fundamental mechanisms, such as facet-dependent behavior (36–40).

Materials and Methods

Synthesis of Pd and Au Nanoparticles. Pd nanocubes were synthesized using 8.0 mL of an aqueous solution containing poly(vinyl pyrrolidone) (PVP, $M_w \approx 55,000$, 105 mg, Aldrich), L-ascorbic acid (AA, 60 mg, Aldrich), and different amounts of KBr and KCl were placed in a 20 mL vial, and preheated in air under magnetic stirring at 80 °C for 10 min. Then, 3.0 mL of an aqueous solution containing Na₂PdCl₄ (57 mg, Aldrich) was added using a pipette. After the vial had been capped, the reaction was allowed to proceed at 80 °C for 3 h. The product was collected by centrifugation and washed 10 times with water to remove excess PVP (19). The synthesis details of Au nanocubes are described elsewhere (41).

In Situ and Ex Situ TEM Characterizations. Closed-cell-type gas environmental transmission electron microscopy was conducted using an Atmosphere 210 System (Protochips Inc.). The instrument was equipped with a specimen rod and a gas supply manifold that can flow in experimental gas up to 1 atm. The specimen rod can accommodate two windowed micro-electro-mechanical system chips. The system can supply the electrical load to one of the chips, which was equipped with a Joule-heating element. The ultrathin silicon nitride microchips were fabricated in-house, where the details are described elsewhere (17). For the in situ TEM experiments without temperature controls (Figs. 1D, 2 A and B, 3, and 4), a pair of ultrathin (≈ 10 nm) SiN_x windowed microchips were used. The thickness of the silicon nitride membrane is measured with variable angle ellipsometry. For the in situ TEM experiment with the temperature controls (Fig. 2C), a small ultrathin (≈ 10 nm) SiN_x windowed microchip is coupled with a large ultrathin (≈ 10 nm) microchip with tungsten Joule-heating elements. The serpentine tungsten heating element is placed at the perimeter of the large microchip to avoid interference when two microchips stacked face-to-face. The tungsten electrode is deposited upon the 150 nm-thick silicon nitride film after the formation of boron-doped silicon support element is created after the differential wet etch. The silicon nitride membrane in this step is deposited thicker than normal ultrathin microchips to provide adequate electrical insulation to tungsten electrode. The 150 nm-thick tungsten was deposited with DC Sputter (AJA international) and annealed at 500 °C vacuum to transform metastable A15 β -phase (1,000 to 10,000 $\mu\Omega$ cm) to body-centered cubic α -phase (10 to 20 $\mu\Omega$ · cm) after the lift-off. To prevent the oxidation, SU-8 2002 epoxy photoresist is covered on the heating element which is present on the perimeter of chip. The final resistance of the heating element has resistance ranging 1700 to 2100 Ω at the room temperature. The 150 nm-thick silicon nitride is later thinned down to ≈ 10 nm with reactive ion etch (RIE) from the top side of the chip. The control of temperature is controlled with Protochips Poseidon Clarity software. The software controls the temperature of membrane by updating the current applied to the Joule heating electrode by measuring the thermal resistance change of electrode with attached potentiostat.

Before assembling the bottom and top chips, we performed plasma treatment to remove any residual hydrocarbon contamination and enhance the wettability. 1 μ L of Pd nanocubes dispersed in isopropyl alcohol solution were drop-casted on the bottom membrane. The windowed chips were stacked facing each other with the fluoroelastomer gasket to make an airtight channel inside of the specimen rod. After purging the cell interior with ultrahigh purity (UHP) argon, 760 torr gas (100% H₂, 100 O₂, or 50% H₂ and 50% O₂ depending on the reaction condition) was flown into the closed cell to initiate the reaction. For the gas channel, SU-8 2002 Epoxy resists which typically have 2.5 to 3.0 μ m of thickness after hard baking were used. The window region will slightly bulge upon the gas flow, and ultimately, the viewing area will have gas channel thickness of 10 μ m (3 + 4 + 4 μ m) (15). The pressure of the gas cell is probed with the pressure gauge directly attached to the outlet of the closed-cell gas cell holder (Protochips Atmosphere 210). In the manuscript, we have denoted the set pressure value which deviates $< \sim 2\%$ to actual pressure for conciseness.

All in situ and ex situ TEM data, including bright-field images, HAADF images, electron diffraction patterns, and EELS maps, were obtained using a JEOL ARM 200CF transmission electron microscope, which was operated at 200 kV. This microscope was equipped with a field-emission gun, probe corrector, Gatan OneView CMOS camera, and a Gatan Image Filter (GIF) system with a K2 Summit electron counting direct detection camera. The energy dispersion was set

to 0.02 eV per channel for the near-edge structure of the O K-edge. The typical dose rate for data acquisition of TEM images and electron diffraction patterns is 5 to 25 e⁻ / (Å²s) to avoid beam-induced effect. The electron dose was measured using K2 Summit electron counting direct detection camera.

DFT Calculations. DFT calculations were used in this study, employing the plane-wave total-energy methodology with the Perdew–Burke–Ernzerhof (PBE) parameterization of the generalized gradient approximation (GGA) for exchange–correlation, as implemented in the Vienna ab initio simulation package (VASP) (42). We used the projector augmented wave (PAW) potentials. The valence electron configurations, 4d¹⁰ for Pd and 1 s¹ for H, were considered here, and the spin polarization method was applied. Unless otherwise specified, all structures were fully relaxed with respect to volume as well as all cell-internal atomic coordinates. We carefully considered and tested the convergence of results with respect to a range of energy cutoff and *k*-points. A plane-wave basis set was used with an energy cutoff of 400 eV to represent the Kohn–Sham wave functions. The summation over the Brillouin zone for the bulk structures was performed on a 6 × 6 × 6 Monkhorst-pack *k*-point mesh for all calculations.

Data, Materials, and Software Availability. All study data are included in the article and/or supporting information.

1. M. Faraday, Experimental researches in electricity. *Philos. Trans. R. Soc.* **122**, 125–162 (1832).
2. S. Sahoo, D. R. Dekel, R. Maric, S. P. Alpay, Atomistic insights into the hydrogen oxidation reaction of palladium–ceria bifunctional catalysts for anion-exchange membrane fuel cells. *ACS Catal.* **11**, 2561–2571 (2021).
3. W. R. W. Daud *et al.*, PEM fuel cell system control: A review. *Renew. Energy* **113**, 620–638 (2017).
4. R. G. Rao *et al.*, Oxygen-doped carbon supports modulate the hydrogenation activity of palladium nanoparticles through electronic metal–support interactions. *ACS Catal.* **12**, 7344–7356 (2022).
5. D. Teschner *et al.*, The roles of subsurface carbon and hydrogen in palladium-catalyzed alkyne hydrogenation. *Science* **320**, 86–89 (2008).
6. L. Wang *et al.*, A sulfur-tethering synthesis strategy toward high-loading atomically dispersed noble metal catalysts. *Sci. Adv.* **5**, eaax6322 (2019).
7. W. Wu, H. Jiang, Palladium-catalyzed oxidation of unsaturated hydrocarbons using molecular oxygen. *Acc. Chem. Res.* **45**, 1736–1748 (2012).
8. A. Schwartz, L. L. Holbrook, H. Wise, Catalytic oxidation studies with platinum and palladium. *J. Catal.* **21**, 199–207 (1971).
9. L. G. Petersson, H. M. Dannetun, I. Lundström, The water-forming reaction on palladium. *Surf. Sci.* **161**, 77–100 (1985).
10. L. G. Petersson, H. M. Dannetun, I. Lundström, Water production on palladium in hydrogen–oxygen atmospheres. *Surf. Sci.* **163**, 273–284 (1985).
11. H. M. Dannetun, D. Söderberg, I. Lundström, L. G. Petersson, The H₂–O₂ reaction on palladium studied over a large pressure range: Independence of the microscopic sticking coefficients on surface condition. *Surf. Sci.* **152–153**, 559–568 (1985).
12. T. A. Germer, W. Ho, Direct characterization of the hydroxyl intermediate during reduction of oxygen on Pt(111) by time-resolved electron energy loss spectroscopy. *Chem. Phys. Lett.* **163**, 449–454 (1989).
13. L. G. Petersson, H. M. Dannetun, I. Lundström, Hydrogen detection during catalytic surface reactions: Evidence for activated lateral hydrogen mobility in the water-forming reaction on pd. *Phys. Rev. Lett.* **52**, 1806–1809 (1984).
14. T. Mitsui, M. K. Rose, E. Fomin, D. F. Ogletree, M. Salmeron, A scanning tunneling microscopy study of the reaction between hydrogen and oxygen to form water on Pd(111). *J. Chem. Phys.* **117**, 5855–5858 (2002).
15. J. Lee *et al.*, Naked-eye observation of water-forming reaction on palladium etalon: Transduction of gas–matter reaction into light–matter interaction. *Photonix* **4**, 20 (2023).
16. K. Koo *et al.*, Advances and opportunities in closed gas-cell transmission electron microscopy. *Chem. Mat.* **36**, 4078–4091 (2024).
17. K. Koo *et al.*, Ultrathin silicon nitride microchip for in situ/operando microscopy with high spatial resolution and spectral visibility. *Sci. Adv.* **10**, ead6417 (2024).
18. F. Manchester, A. San-Martin, J. Pitre, The H–Pd (hydrogen–palladium) system. *J. Phase Equilibria* **15**, 62–83 (1994).
19. M. Jin *et al.*, Synthesis of Pd nanocrystals enclosed by 100 facets and with sizes <10 nm for application in CO oxidation. *Nano Res.* **4**, 83–91 (2011).
20. D. Tabor, *Gases, Liquids and Solids: And Other States of Matter* (Cambridge University Press, 1991).
21. J. K. Edwards, S. J. Freakley, A. F. Carley, C. J. Kiely, G. J. Hutchings, Strategies for designing supported gold–palladium bimetallic catalysts for the direct synthesis of hydrogen peroxide. *Acc. Chem. Res.* **47**, 845–854 (2014).
22. S. Yu *et al.*, High activity and selectivity of single palladium atom for oxygen hydrogenation to H₂O₂. *Nat. Commun.* **13**, 4737 (2022).
23. G. H. Han, S. H. Lee, S. Y. Hwang, K. Y. Lee, Advanced development strategy of nano catalyst and DFT calculations for direct synthesis of hydrogen peroxide. *Adv. Energy Mater.* **11**, 2003121 (2021).
24. K. A. Unocic *et al.*, Introducing and controlling water vapor in closed-cell in situ electron microscopy gas reactions. *Microsc. Microanal.* **26**, 229–239 (2020).
25. G. Brown Jr., G. Waychunas, J. Stohr, F. Sette, Near-edge structure of oxygen in inorganic oxides: Effect of local geometry and cation type. *Le Journal de Physique Colloques* **47**, C8-685–C8-689 (1986).
26. D. Wallis, P. Gaskell, R. Brydson, Oxygen K near-edge spectra of amorphous silicon suboxides. *J. Microsc.* **180**, 307–312 (1995).
27. N. Luhmann *et al.*, Effect of oxygen plasma on nanomechanical silicon nitride resonators. *Appl. Phys. Lett.* **111**, 063103 (2017).
28. S. Myneni *et al.*, Spectroscopic probing of local hydrogen-bonding structures in liquid water. *J. Condens. Matter Phys.* **14**, L213 (2002).
29. L.-Å. Näslund *et al.*, X-ray absorption spectroscopy study of the hydrogen bond network in the bulk water of aqueous solutions. *J. Phys. Chem. A* **109**, 5995–6002 (2005).
30. G. R. Wight, C. E. Brion, K-shell excitation of CH₄, NH₃, H₂O, CH₃OH, CH₃OCH₃ and CH₃NH₂ by 2.5 keV electron impact. *J. Electron Spectros. Relat. Phenomena* **4**, 25–42 (1974).
31. S. M. Ghodsi, S. Anand, R. Shahbazian-Yassar, T. Shokuhfar, C. M. Megaridis, In situ study of molecular structure of water and ice entrapped in graphene nanovessels. *ACS Nano* **13**, 4677–4685 (2019).
32. J. B. MacNaughton, L.-Å. Näslund, T. Anniyev, H. Ogasawara, A. Nilsson, Peroxide-like intermediate observed at hydrogen rich condition on Pt(111) after interaction with oxygen. *Phys. Chem. Chem. Phys.* **12**, 5712–5716 (2010).
33. G. Scatchard, G. M. Kavanagh, L. B. Ticknor, Vapor–liquid equilibrium. VIII. Hydrogen peroxide–water mixtures. *J. Am. Chem. Soc.* **74**, 3715–3720 (1952).
34. M. Boudart, H. S. Hwang, Solubility of hydrogen in small particles of palladium. *J. Catal.* **39**, 44–52 (1975).
35. T. C. Narayan *et al.*, Direct visualization of hydrogen absorption dynamics in individual palladium nanoparticles. *Nat. Commun.* **8**, 14020 (2017).
36. Z. Yin *et al.*, Visualization of facet-dependent pseudo-photocatalytic behavior of TiO₂ nanorods for water splitting using in situ liquid cell TEM. *Nano Energy* **62**, 507–512 (2019).
37. G. De Gregorio *et al.*, Facet-dependent selectivity of Cu catalysts in electrochemical CO₂ reduction at commercially viable current densities. *ACS Catalysis* **10**, 4854–4862 (2020).
38. N. Johnson *et al.*, Facets and vertices regulate hydrogen uptake and release in palladium nanocrystals. *Nature Mater.* **18**, 454–458 (2019).
39. W. Dong, V. Ledentu, P. Sautet, A. Eichler, J. Hafner, Hydrogen adsorption on palladium: A comparative theoretical study of different surfaces. *Surface Sci.* **411**, 123–136 (1998).
40. V. J. Bukas, K. Reuter, A comparative study of atomic oxygen adsorption at Pd surfaces from Density Functional Theory. *Surface Sci.* **658**, 38–45 (2017).
41. M. N. O'Brien, M. R. Jones, K. A. Brown, C. A. Mirkin, Universal noble metal nanoparticle seeds realized through iterative reductive growth and oxidative dissolution reactions. *J. Am. Chem. Soc.* **136**, 7603–7606 (2014).
42. G. Kresse, J. Furthmüller, Efficient iterative schemes for ab initio total-energy calculations using a plane-wave basis set. *Phys. Rev. B* **54**, 11169–11186 (1996).

ACKNOWLEDGMENTS. We acknowledge the support on gas cell chip fabrication from the Air Force Office of Scientific Research (AFOSR) with the grant number of AFOSR FA9550-22-1-0300. The hydrogen-related work was partly supported by the HEISs (DE-SC0023450), an Energy Frontier Research Center funded by the U.S. Department of Energy, Office of Science. This work made use of the EPIC facility of Northwestern University's NUANCE Center, which has received support from the Soft and Hybrid Nanotechnology Experimental (SHyNE) Resource (NSF ECCS-2025633); the MRSEC program (NSF DMR-2308691) at the Materials Research Center; the International Institute for Nanotechnology (IIN). We would like to thank Professor David Seidman at Northwestern University for the helpful discussion. Y.L. would like to acknowledge the support from the IIN Ryan fellowship.

Author affiliations: ^aDepartment of Materials Science and Engineering, Northwestern University, Evanston, IL 60208; ^bInternational Institute of Nanotechnology, Northwestern University, Evanston, IL 60208; ^cThe Northwestern University Atomic and Nanoscale Characterization Experimental (NUANCE) Center, Northwestern University, Evanston, IL 60208; and ^dDepartment of Physics, Technical University of Denmark, Kongens Lyngby 2800, Denmark

Author contributions: Y.L., K.K., X.H., and V.P.D. designed research; Y.L., K.K., Z.M., X.F., and X.H. performed research; Y.L., K.K., Z.M., X.F., X.H., and V.P.D. analyzed data; and Y.L., K.K., and V.P.D. wrote the paper.